High Energy, Long Cycle Life Lithium-ion Batteries for PHEV Application

Donghai Wang, Principle Investigator
Pennsylvania State University
328 Reber Building
University Park, PA 16802
Phone: (814) 863-1287; Fax: (814) 863-4848
E-mail: dwang@psu.edu

Adrienne Riggi, DOE Project Manager
National Energy Technology Laboratory
3610 Collins Ferry Road
Morgantown, WV 26507
Phone: (304)285-5223;
E-mail: Adrienne.Riggi@NETL.DOE.GOV

Start Date: October 2014
End Date: September 30 2016

I.1.A.1. Abstract

Objectives

- Demonstrate a 2.5 Ah prismatic Li-ion cell capable of 1) an energy density of 330 Wh/kg (770 Wh/L) at C/3 rate; 2) a power density of 1600 W/L while maintaining an energy density above the DOE PHEV goal of 200 Wh/kg; 3) a long cycle life with 95% capacity retention in 500 cycles at C/3 and 1C rate at 80% depth of discharge (DOD).

Technical barriers

- The development of the proposed Li-ion battery presents technical barriers for each of the system's components: anode, cathode, binder, and electrolyte. Although silicon-alloy anode materials have shown remarkable capacities above 2000 Ah/g, the silicon will undergo large volume change (~400%) upon lithiation/delithiation. In effect, other issues arise including unstable SEI, pulverization and aggregation of the Si particle, and low coulombic efficiency (less than 99.8%) compared with graphite (higher than 99.9%). Furthermore, layered oxide cathode materials will need to overcome a relatively low practical capacity (~170 mAh/g), along with other issues such as chemical and structural instability, transition metal dissolution, and transition metal redox potential changes. The technical barriers for the anode and cathode may partially be addressed with an appropriate binder/electrolyte, however the chemical composition of these components must be optimized to ensure compatibility.

Accomplishments

- The optimization of structure, particle size and surface coating of PSU Si-graphite anode material have been completed
- Optimized PSU Si-graphite material has been scaled up (~500 g)
- The high-loading (6.5 mg/ cm2) electrode using a cross-linked binder with great quality has been fabricated
- The specific capacity, mass loading and binder content of PSU Si-graphite anode has been optimized
- The areal capacity, cyclability, electrolyte additives, voltage window of PSU Si-graphite anode have been optimized using the full pouch cell for the full cell construction.

- A diversity of performance modification strategies has been utilized to suppress the degradation of Ni-rich cathode materials and to improve their overall electrochemical performance.
- One kilogram of the optimized concentration-gradient (CG) cathode material $LiNi_{0.76}Co_{0.10}Mn_{0.14}O_2$ has been prepared with good control of composition, morphology, and electrochemical performance, which delivered an initial specific capacity close to 190 mA h g^{-1} at C/10 and 180 mA h g^{-1} at C/3 as well as good cyclability in pouch-type graphite full cells with a 4.4 upper voltage cut-off.
- Scalable SLMP coating method on electrodes is developed through a polymer solution system. The system is optimized through the selection of solvent, polymer binder and polymer concentration. The optimized binder solution is 1% concentration of polymer binder in xylene, and the polymer binder is chosen as the mixture of poly(styrene-co-butadiene) rubber (SBR) and polystyrene (PS). The effect of SLMP is demonstrated through both half coin cells and full pouch cells.
- A series of electrolyte containing fluorinated cyclic carbonates as the anode SEI former with trifluoroethyl methyl carbonate (F-EMC) and LiPF6 has been designed, synthesized and evaluated.
- Full cells fabrication, activation and pre-test have been carried out. Three kind of cells have been prepared as follow: unlithiated PSU Si-graphite anode | NCM523 cathode, unlithiated PSU Si-graphite anode | UTA cathode and lithiated PSU Si-graphite anode | NCM523 cathode.

Future Achievements

- Further optimization of the full pouch cell using PSU Si-graphite anode and UTA Ni-rich oxide cathode
- Further improvements of the first cycle efficiencies of high-loading and high-capacity PSU Si-graphite anode and UTA Ni-rich oxide cathode
- Further enhancement of the uniformity and effect of SLMP prelithiation for high-loading and multilayered full pouch cell

✧ ✧ ✧ ✧ ✧

I.1.A.2. Technical Discussion

Background

With a relatively high energy density and long lifespan, Li-ion batteries have become the state-of-the-art and widely-adopted power technology for plug-in hybrid electric vehicle (PHEV), electric vehicle (EV), and other portable electronic devices. However, the popularity of the current PHEVs and EVs in our daily life is being seriously hindered by their high cost, limited travelling distance, and restrained vehicle size, mainly due to the lack of high-performance and cost-effective lithium-ion batteries.

Introduction

In effect, research in the field of battery chemistry has focused on the development of advanced battery components that will significantly improve the practical performance of Li-ion batteries. Within the last decade, the performances of the primary components - cathode, anode, binder, and polymer - have been enhanced through careful modification in chemical composition, although often independent of each other. In this regard, a collaborative effort is needed to improve the overall performance of Li-ion batteries by enhancing individual battery components simultaneously, so that a high-performance, cost-effective Li-ion battery able to satisfy diverse demands, especially transportation, can be achieved.

Approach

The development of a high energy/power Li-ion battery suitable for PHEV and EV applications can be accomplished through the expertise and experience of a multiple organizational team with facilities and collaboration spanning Penn State University (PSU), University of Texas at Austin (UT-Austin), Lawrence Berkley National Laboratory (LBNL), Argonne National Laboratory (ANL), and industrial partner EC Power (ECP). PSU and UT-Austin will use extensive knowledge in the state-of-the-art anode and cathode materials, respectively, to develop optimized and compatible electrodes in the Li-ion battery. Innovative polymer binders/ anode prelithiation and electrolytes solutions will be developed by LBNL and ANL, respectively, based on their well-established expertise in this area. Finally, the culmination of these state-of-the-art battery components will be realized through the intelligent cell design and fabrication techniques of ECP.

Results

We have achieved the following progress:

Anode

1. PSU cross-linked binders have been developed, enabling fabrication of high quality Si anodes with good performance.

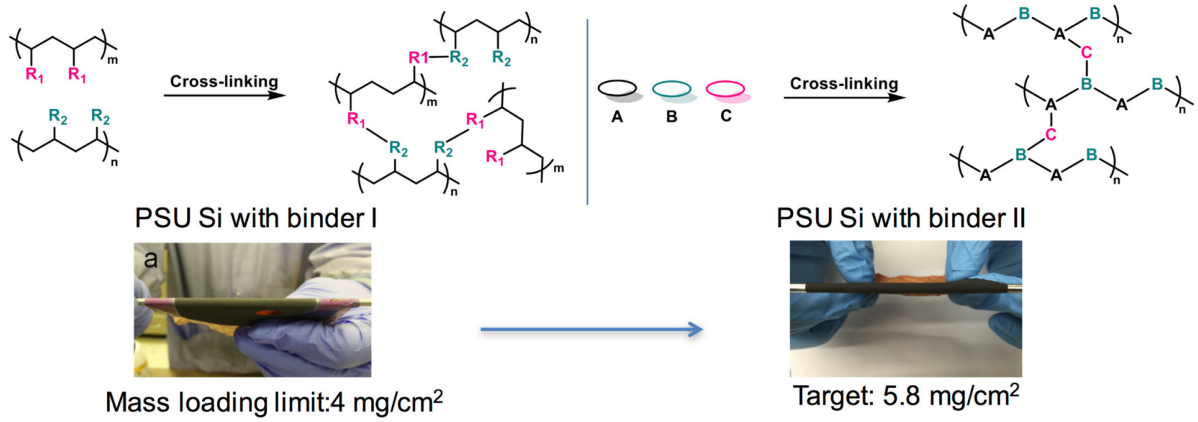

Figure I-1: PSU cross-linked binders for high-loading PSU Si-graphite anodes. The left binary cross-linked binder enables good electrode quality with the active material mass loading of 4 mg/ cm² and the right ternary cross-linked binder pushes the mass loading to 5.8 mg/ cm² with great quality.

To develop the PSU Si-graphite anode with a high areal capacity, we need to push the mass loading of active material of the electrode to a very high level (~5.8 mg/ cm^2) and the electrode quality should be good enough for the full cell operation. As shown in **Figure I-1**, we have been developed two kinds of cross-linked binders, which are binary and ternary cross-linking polymers. The mass loading of the PSU Si-graphite anode using binary binder I can be pushed up to 4 mg/ cm^2, while the one of ternary binder II shows great quality with the mass loading of 5.8 mg/ cm^2. This is adequate for our full cell operation design. The Si-graphite anode using the ternary binder II exhibits good cyclability in half-cell system (Figure I-2). The area capacity has been reached to 4.9 mAh/ cm^2.

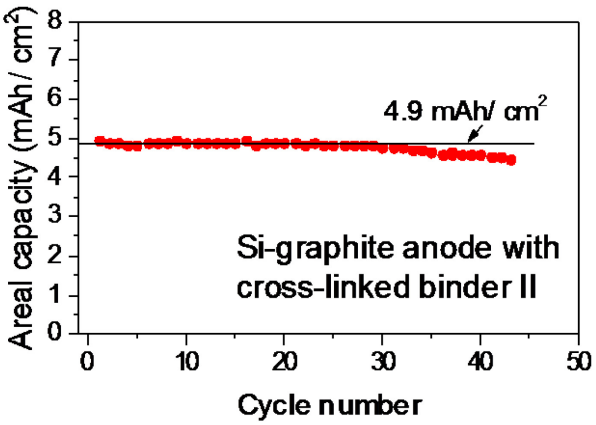

Figure I-2: Half-cell performance of Si-graphite anode with ternary binder II. The mass loading is 5.8 mg/ cm².

2. PSU Si-graphite material scale-up and electrode fabrication.

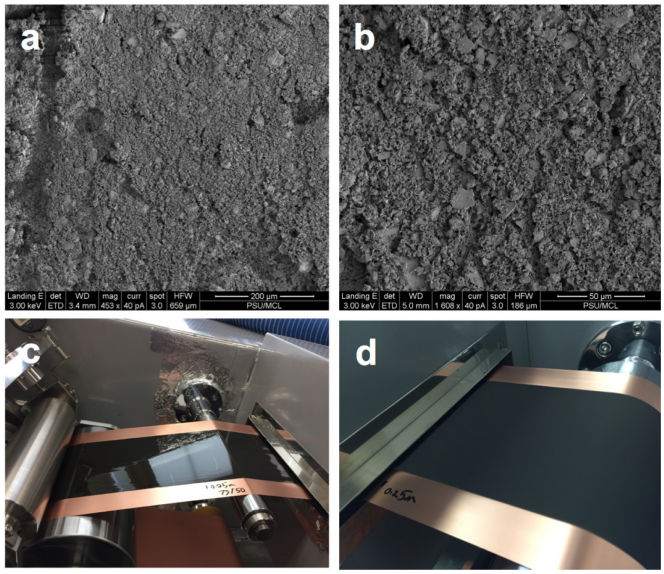

Figure I-3: Material fabrication and electrode fabrication of PSU Si-graphite. a,b, SEM images of Si materials with uniform particle size. c,d, High-quality electrode using Si-graphite material and ternary binder II.

After optimizing the Si structure and surface layer, we have completed the material scale-up and are able to prepare 500 g Si material every single batch. The Si particle size has also been screened to ensure the uniform particle size. The electrode also presents very good quality before and after heat treatment.

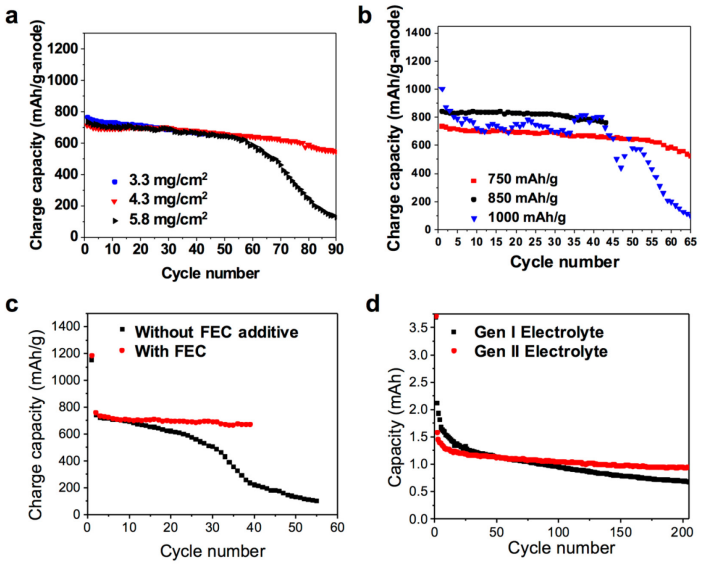

Figure I-4: PSU Si-graphite anode optimization including a) mass loading of active material, b) specific capacity, c) electrode with FEC additives and d) electrode with different electrolyte systems.

3. Electrochemical optimization of the PSU Si-graphite anode in half- cell and full- cell systems

The electrochemical performances of PSU Si-graphite including mass loading, specific capacity, electrolyte and additives have been optimized I the half-cell systems. As shown in Figure I-3, PSU Si-graphite electrodes with mass loading of 5.8 mg/ cm^2 shows similar capacity with the ones of low loadings, indicating good electrode structure and conductivity. By tuning the ratio of Si and graphite, we demonstrate that the electrode which delivers a charge capacity of 850 mAh/ g, presents best cyclability. Moreover, the compatibility of the material with electrolyte and additives has also been studied. The Gen II electrolyte with FEC additive exhibits the optimized cell performance and is used for the full cell operation. The FEC has been proved to be very important for the Si-graphite electrode with high mass loading.

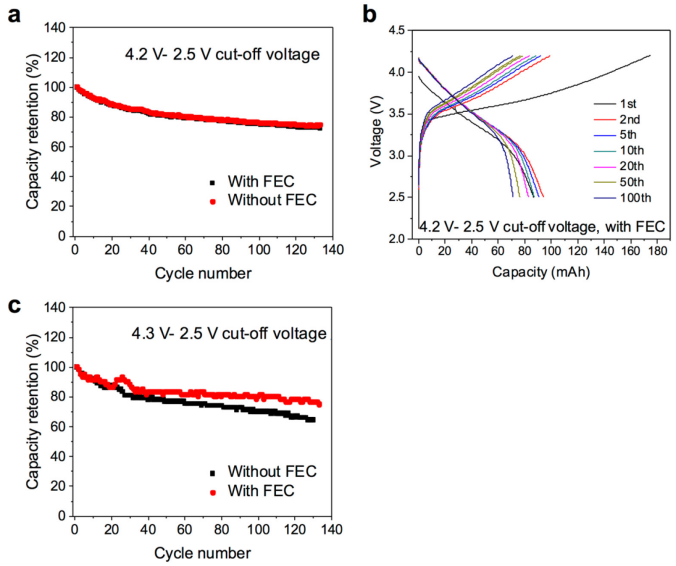

Figure I-5: Full-cell performance optimization including additives and voltage window with the double-layer pouch cell system.

Using the optimized electrode structure and electrolyte, the full-cell performance has been optimized with the double-layer pouch cell system. PSU Si-graphite anode is paired with commercial NCM523 cathode with a 1:1 N/P ratio. As shown in Figure I-5a, both cells with/ without FEC additive show good performance under the voltage window of 4.2 –2.5V. However, when changing the voltage window to 4.3 –2.5V, the one with FEC additive shows much better performance with a 73% capacity retention after 130 cycles.

Cathode

1. Understanding the degradation processes of Ni-rich $LiNi_{0.7}Co_{0.15}Mn_{0.15}O_2$ during cycling

As a very promising high-performance cathode material, Ni-rich materials attract great attention from both academia and industry. However, the Ni-rich compositions generally show poor cyclability, hindering their wide applications. Therefore, it is of great importance to understand the various degradation processes of nickel-rich materials, so that more specific and effective methods can be adopted to improve their overall performance. We prepared a baseline material $LiNi_{0.7}Co_{0.15}Mn_{0.15}O_2$ (denoted as NCM 71515) and its electrochemical performance in lithium half-cells was obtained at room temperature with a cut-off voltage of 4.5 V *vs*. Li/Li^+. The sample delivered a discharge capacity close to 190 mA h g^{-1} and also showed notable voltage and capacity fade during cycling. It is generally believed that the capacity fading mechanism of Ni-rich layered oxides is linked to the rapid degradation of electrode/electrolyte interface that induces large over-potentials during both charge-discharge processes as cycling proceeds and to the structural instability at the highly charged state during cycling, while the bulk remains largely intact and undamaged.

Figure I-6a illustrates the TOF-SIMS depth profiles of the baseline sample after 100 charge-discharge cycles. These profiles of the secondary ions of interest, such as LiF_2^-, are referenced to those obtained from the pristine electrode, and they reveal the complex multi-layer characteristics of the surface chemistry of Ni-rich layered oxide electrodes during high-voltage electrochemical operation, as proposed theoretically in the literature. Importantly, we notice degradation products including: (i) LiF, represented by LiF_2^-, appearing mostly localized at the very surface of the electrode, the first layer, and also rich in the subsequent second layer; (ii) MnF_2, signified by MnF_2^-, showing the highest concentration in the second layer; and (iii) NiO, indicated here by the NiO^- to Ni^- ratio, emerging in the third layer. These three "layers" correspond to the various aspects of electrochemical degradation at the surface of Ni-rich layered oxide electrodes in the common EC-DEC/$LiPF_6$ solutions: (i) deposition of various solvent and salt decomposition products from the electrolyte, (ii) active mass dissolution aggravated by acidic species attack (*e.g.*, HF – generated in the presence of a trace amount of electrolyte impurities such as H_2O), and (iii) intrinsic surface structural reconstruction from the layered to 'rock-salt' phase due to destabilized Ni-ion migration towards neighboring Li layers in the highly delithiated state.

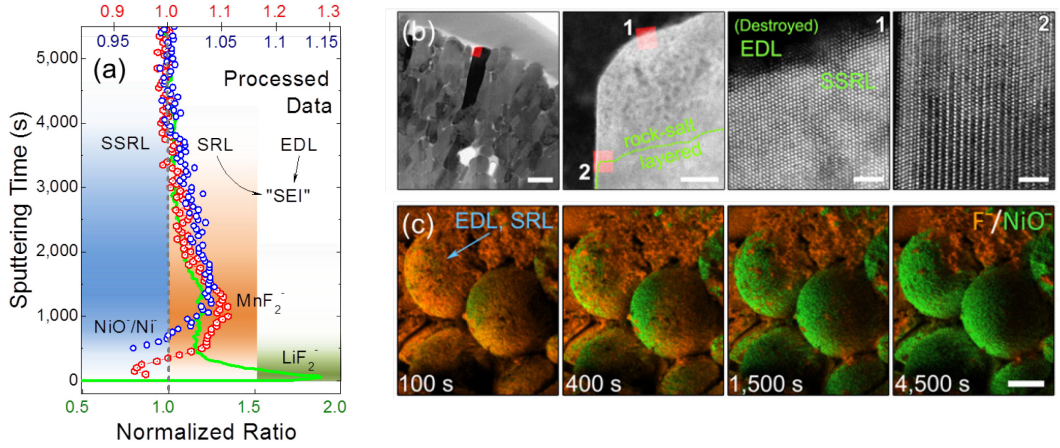

Figure I-7: (a) TOF-SIMS depth profiles of various chemical species from the surface of the baseline NCM 71515 composite electrodes after 100 cycles at room temperature, referenced with the pristine electrode (not shown here) as a function of sputtering time; and visualization of the surface degradation of NCM 71515 electrodes after 100 cycles. (b) HAADF-STEM images showing the local structure at the primary particle surface; the scale bars are 400, 20, 2, and 2 nm from left to right;

(c) TOF-SIMS mappings showing the composite electrode surface with cathode secondary particles, additive carbon, and binder; the scale bar is 10 µm.

In this work, we refer to the aforementioned three 'layers' as an electrolyte deposition layer (EDL), a surface reaction layer (SRL), and a surface structural reconstruction layer (SSRL), respectively, as shown in Figure I-6a. In Figure I-6b, HAADF-STEM images reveal the local structure of the cycled NCM 71515 primary particle surface. A clear boundary is shown between the pristine layered $R\bar{3}m$ structure and the irreversibly formed rock-salt $Fm\bar{3}m$ phase (SSRL) during cycling, with distinctly differing thickness along different crystal orientations. It is expected that the SSRL formation is promoted along the lithium diffusion pathway in the layered matrix of Ni-rich layered oxides. Of particular note, the surface organic deposits due to electrode-electrolyte reactivity are largely nonexistent in the HAADF-STEM images due to their highly sensitive nature towards the high-energy electron-beam irradiation. Important also is a considerable difficulty in the elimination of ambient air-exposure-induced artifacts during the sample preparation for high-resolution STEM. Consequently, illustrative TOF-SIMS high-resolution mappings were collected on the same sample as a function of etching depth, as seen in Figure I-6c. In the figure, maps of the electrode along the *x-y* planes demonstrate that the surface of the particles (represented by the NiO^- fragment), initially entirely covered by the degradation-induced chemical functional groups (represented by F^-), gradually emerges upon Cs^+ etching.

For further detailed and comprehensive visualization in three dimensions of the chemical alterations occurring on the electrode surface, a series of TOF-SIMS maps of various organic and inorganic species were collected on the cycled baseline NCM 71515 sample **(**Figure I-7**)**. In the upper two rows of Figure I-7, complex surface deposits in EDL, represented by cumulative signals of C_2^-, POF_2^-, and LiF_2^- fragments projected along the x-y planes prior to and after intensive sputtering, are unequivocally visualized. Not surprisingly, signal counts of most of these fragments are reduced nearly uniformly on the entire electrode during etching. Also shown are the surface corrosion products in SRL evidenced by LiF_2^-, Ni^-, and MnF_2^- ions. In contrast to the EDL species, these fragments show substantial decrease in intensity at the cathode particles, since the additive carbon and binder in the composite electrode do not react with HF. Apparently, the degradation products are mostly located at the surface of the secondary particles, although electrolyte penetration along with further attack through micro-cracks towards the interior of particles is possible. Notably, several maps of O^-, Ni^-, Li^-, MnF^{2-}, etc. in the bottom row of Figure I-7reveal the complex surface chemistry on carbon additives, which is believed to be mostly the result of the active mass dissolution. During migration within the electrolyte, these dissolved compounds make their ways to the conductive carbon surface and eventually through the separator to the anode. The precipitation of the dissolved products from the common cathode materials on the graphite anode as well as conductive carbon additives at the cathode side are recognized as a key limiting factor for the cycle life in existing lithium-ion batteries. Upon closer inspection, it was also noticed that the NiO phase (NiO^-) appears rich at the exterior of a secondary particle whereas Li (Li^-) is more concentrated at the core (Figure I-7, bottom). This further corroborates that the electrochemical degradation for Ni-rich layered oxides tends to be more localized at the secondary particle's surface.

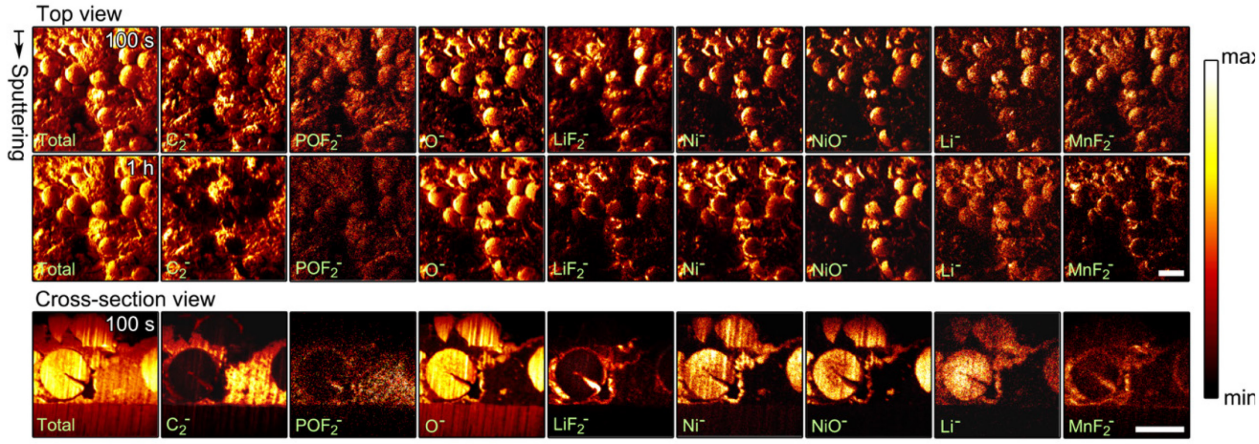

Figure I-7: Two-dimensional TOF-SIMS mapping of baseline NCM 71515 composite electrodes after 100 cycles, revealing various surface degradation products at the secondary particle surface as well as additive carbon and polymeric binder. Upper two rows are top views collected after 100 s- and 1 h-Cs^+ etching, while the bottom row is taken from the cross-sectional perspective (100 s-Cs^+ etching). From left to right, the secondary ions of interest are total, C^{2-}, C_2P^-, POF^{2-}, O^-, LiF^{2-}, Ni^-, NiO^-, Li^-, and MnF^{2-}, respectively. The scale bars are both 20 µm.

2. Performance enhancement of Ni-rich materials

The degradation mechanism research above indicates that the performance improvement of Ni-rich materials primarily lies in the enhancement of their surface chemical and structural stability. On the basis of this, several strategies were used to achieve this goal, including compositional alteration, element doping, surface coating, and the combination of materials.

2.1 Effect of Mn substitution for Ni in $LiNi_{0.8-x}Co_{0.10}Mn_{0.1+x}O_2$

Rate performance of the $LiNi_{0.8-x}Co_{0.1}Mn_{0.1+x}O_2$ cathodes with different Mn contents is presented in Figure I-8. The $LiNi_{0.76}Co_{0.10}Mn_{0.14}O_2$ sample shows higher discharge capacities at various C rates. $LiNi_{0.72}Co_{0.10}Mn_{0.18}O_2$ shows slightly poor rate capability as compared to $LiNi_{0.76}Co_{0.10}Mn_{0.14}O_2$, probably due to the reduced conductivity of the electrode caused by the increase in Mn content. From the charge/discharge voltage profiles at different C rates, it can be found that the $LiNi_{0.80}Co_{0.10}Mn_{0.10}O_2$ sample shows discharge voltage profiles with dramatically reduced working voltage at high C rates Figure I-8b, indicating a significant increase in internal resistance and an obvious energy fade when operating at increased current densities, which is undesired for practical applications. In contrast, both $LiNi_{0.72}Co_{0.10}Mn_{0.18}O_2$ and $LiNi_{0.76}Co_{0.10}Mn_{0.14}O_2$ exhibit limited decay in the working voltage even at 5 C discharge rate, demonstrating the improved structural stability and rate capability of materials with relatively higher Mn contents.

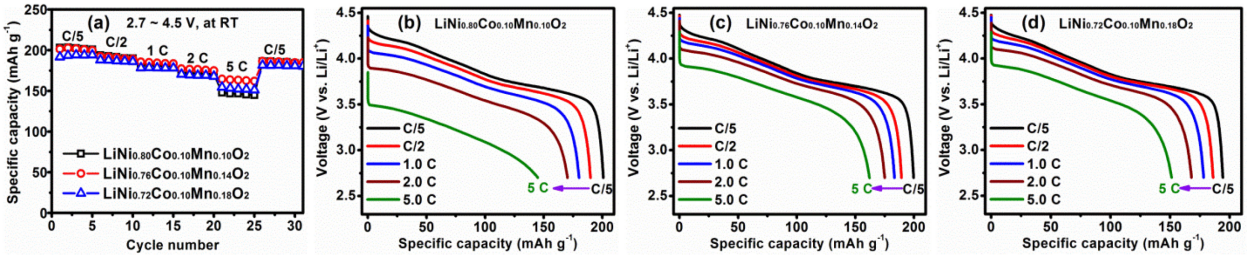

Figure I-8: (a) Rate performance of the $LiNi_{0.8-x}Co_{0.1}Mn_{0.1+x}O_2$ materials at room temperature and the corresponding discharge profiles of (b) $LiNi_{0.80}Co_{0.10}Mn_{0.10}O_2$, (c) $LiNi_{0.76}Co_{0.10}Mn_{0.14}O_2$, and (d) $LiNi_{0.72}Co_{0.10}Mn_{0.18}O_2$ at different C rates in the range of 2.7 - 4.5 V.

To get insight into the good structural stability of the material with high Mn content, electrochemical impedance spectroscopy (EIS) analysis was carried out to study the interfacial electrochemistry and reaction kinetics of the $LiNi_{0.8-x}Co_{0.10}Mn_{0.1+x}O_2$ cathode materials at the charged state of 4.3 V (Figure I-9 (Left)). Upon cycling, the passivation surface-film resistance and the charge-transfer resistance of the high-Mn-content cathode is considerably lower than those of the low-Mn-content cathode, ascribed to the stabilization of the $LiNi_{0.72}Co_{0.10}Mn_{0.18}O_2$ electrode surface in the presence of higher Mn contents. After 50 cycles, $LiNi_{0.72}Co_{0.10}Mn_{0.18}O_2$ exhibits a low surface layer resistance, indicating a thinner passivation film accumulated on the electrode surface. Meanwhile, the charge-transfer resistance of the $LiNi_{0.72}Co_{0.10}Mn_{0.18}O_2$ electrode is also much smaller than that observed for the $LiNi_{0.8}Co_{0.10}Mn_{0.1}O_2$ electrode over the same period of cycling. The stable interfacial resistances in the $LiNi_{0.72}Co_{0.10}Mn_{0.18}O_2$ electrode reflect an improved quality of electrode/electrolyte interface. The high Mn content at the particle surface stabilizes the interface during cycling, resulting in better electrochemical performance. The $Li_{1-\delta}Ni_{0.72}Co_{0.10}Mn_{0.18}O_2$ electrode exhibits an exothermic reaction with the peak located at a higher temperature of 229 ℃ compared to that of $Li_{1-\delta}Ni_{0.8}Co_{0.10}Mn_{0.1}O_2$ (221 ℃) (Figure I-9 (Right)). Also, the exothermic heat generated with $Li_{1-\delta}Ni_{0.72}Co_{0.10}Mn_{0.18}O_2$ is lower (527 J g^{-1}) than that with $Li_{1-\delta}Ni_{0.8}Co_{0.10}Mn_{0.1}O_2$ (721 J g^{-1}), indicating that higher Mn content, especially in the particle outer layer, significantly enhances the thermal stability of the Ni-rich cathodes.

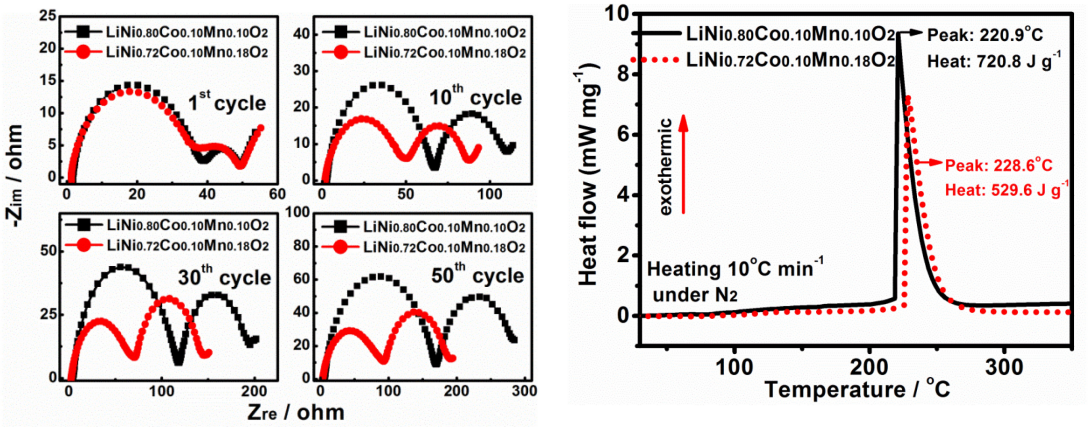

Figure I-10: Left, Nyquist Plots of the $LiNi_{0.8-x}Co_{0.10}Mn_{0.1+x}O_2$ materials in thick electrodes at the charged state of 4.3 V during cycling at C/3 rate after 3 formation cycles at C/5 rate, Right, DSC profiles of the $Li_{1-\delta}Ni_{0.8-x}Co_{0.10}Mn_{0.1+x}O_2$ electrodes at the charged state of 4.5 V.

2.2 Effect of Al doping on the performance of Ni-rich material

Improving the cycling stability of Ni-rich cathode materials is one of the major goals in this project. One of the effective strategies is elemental doping. Thus, Al-doped $LiNi_{0.81}Co_{0.14}Al_{0.05}O_2$ (NCA) was prepared via a two-step method: transition-metal co-precipitation of $Ni_{0.85}Co_{0.15}(OH)_2$ and subsequently 5 mol. % Al doping during the lithiation heat treatment. Also, $LiNi_{0.85}Co_{0.15}O_2$ was prepared for a comparison.

The electrochemical performance of NCA was first recorded in coin-type Li half cells at room temperature and then in pouch full cells. Figure I-10a compares the cycling stability of the two samples in the voltage window of 3.0–4.5 V at C/5 using the standard 1.0 M $LiPF_6$/EC-DEC electrolyte. As shown, both samples delivered high initial specific discharge capacities of slightly above 200 mA h g^{-1} (203 mA h g^{-1} for NCA, 201 mA h g^{-1} for NC8515), common for Ni-rich layered oxides with Ni incorporation above 0.8. Not surprisingly, the $LiNi_{0.85}Co_{0.15}O_2$ sample demonstrates rather poor cycling performance under high-voltage cell operation, with capacity rapidly decreasing to around 50% after 100 charge-discharge cycles. The Al-doped NCA cathode, on the other hand, demonstrates notable improvement in the cycling stability, and a capacity retention of 93.6% was achieved after 100 cycles, much higher than that of $LiNi_{0.85}Co_{0.15}O_2$. Further evidence of the voltage stability of NCA cathode is shown in Figure I-10b. It can be seen that charge-discharge over-potentials remain relatively stable over the course of 200 cycles. Also, the capacity retention of the sample is still ~ 88% after 200 cycles. The full-cell testing of NCA cycled between 2.5 and 4.4 V under C/3 in Figure I-10c, clearly shows the desired cyclability, with a capacity retention of 92.0% after 250 cycles. These results indicate that Al doping is very effective in prolong the cycle life of Ni-rich layered oxide cathode materials.

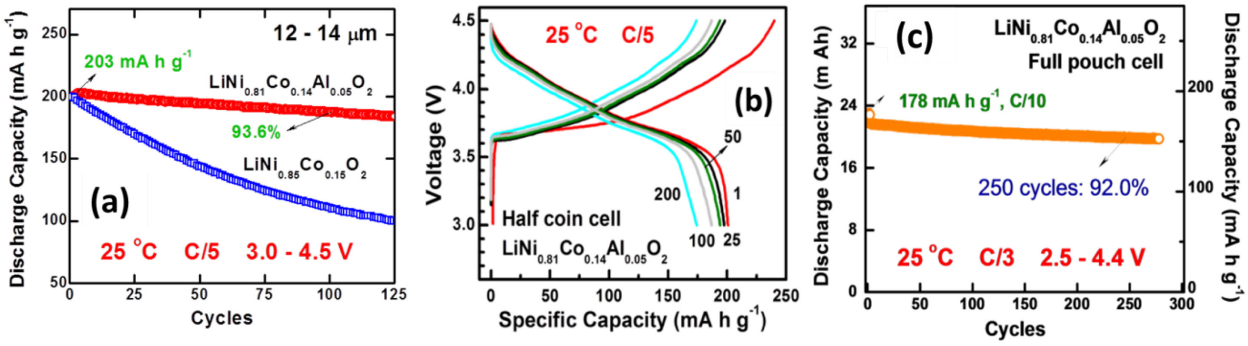

Figure I-10: (a) Evolution of discharge capacities of the two samples as a function of cycles in coin-type Li half cells, (b) galvanostatic electrochemical profiles, and (c) cycling test of $LiNi_{0.81}Co_{0.14}Al_{0.05}O_2$ in pouch-type full cells.

2.3 Effect of surface coating on the performance of Ni-rich material

Surface coating is regarded as an effective method of enhancing surface stability of cathode materials. Investigated is the effect of several coating materials and coating structure on the performance of Ni-rich cathode material. All of them have proven effective in improving the performance of Ni-rich materials.

To enhance the surface stability of the Ni-rich $LiNi_{0.7}Co_{0.15}Mn_{0.15}O_2$ cathode, Li_2ZrO_3 has been coated on the particles' surfaces as a protective agent by two methods: sol-gel and precipitation. Inspired by the thermodynamic mechanisms of solid-state diffusion of transition-metal ions at high temperatures, two sintering temperatures of 650 and 800 °C were chosen to investigate the possible bi-functional effects of doping and coating under different sintering conditions. Figure I-11 presents a comparative cross-sectional SEM-EDX mapping of the Zr element of all samples. Two observations are to be noted as important. First, the most uniform distribution of Zr at one secondary particle's surface was achieved by the precipitation method, followed by sintering at 650 °C. Second, the most uniform doping of Zr^{4+} into the local lattice at one secondary particle was achieved by sol-gel method, followed by sintering at 800 °C. Besides, the other two preparation conditions cause an aggregation of Zr to a certain extent at one secondary particle's surface. The reason for such variations in Zr distribution could be understood as follows: first, sol-gel leads to surface coating of Li^+ and Zr^{4+} agents on primary particles while precipitation leads to the secondary particle's coating; second, 650 and 800 °C sintering temperatures result in different levels of elemental diffusion across the particles.

Figure I-11 also shows the capacity retention during 100 cycles of all samples. Apparently, the Li_2ZrO_3-coated $LiNi_{0.7}Co_{0.15}Mn_{0.15}O_2$ cathodes prepared by precipitation and after sintering at 650 °C provides the best cyclability compared to others, *i.e.*, 92.2, 92.8, and 97.7% capacity retention with respect to 1, 3, and 5 wt.% of coating agent. This observation agrees well with the conclusion from SEM-EDX mapping that the most uniform coating of Zr on one secondary particle could provide the most efficient protection from corrosive electrolyte. The results indicate that Li_2ZrO_3 can improve the cyclability of Ni-rich material effectively.

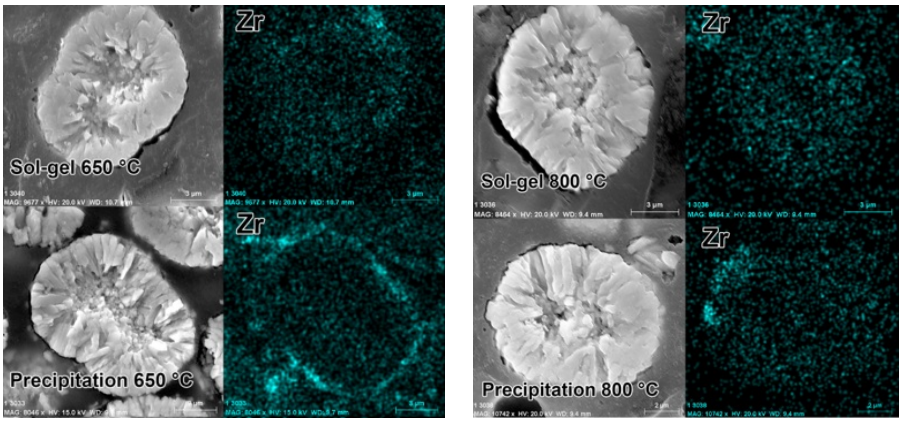

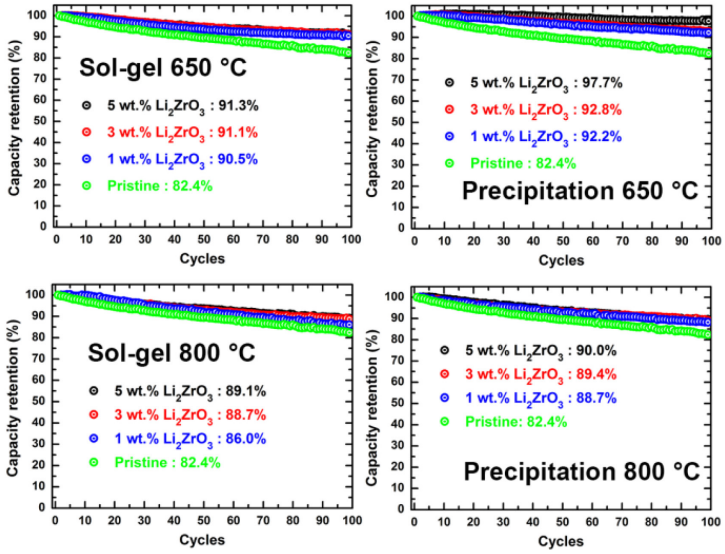

Figure I-12: Cross sectional SEM-EDX mapping of the Zr element in the Li_2ZrO_3-coated $LiNi_{0.7}Co_{0.15}Mn_{0.15}O_2$ samples prepared by sol-gel and precipitation methods and capacity retention of the Li_2ZrO_3-coated $LiNi_{0.7}Co_{0.15}Mn_{0.15}O_2$ cathodes prepared by sol-gel and precipitation methods with a cycling condition of 3.0 – 4.5 V, C/3 rate, and 25 °C.

Besides the single coating, a double coating strategy was also adopted, aiming to enhance the surface stability of Ni-rich materials without the expense of specific capacity. To stabilize the surface of the Ni-rich material, we pursued Li-rich material coating on Ni-rich oxides. Note that, in general, Li-rich materials show more stable cycle performance compared to Ni-rich materials when they are cycled at above 4.5 V. In this regard, Li-rich material is a good coating material for Ni-rich materials, which can reduce the surface instability of Ni-rich materials. Figure I-12 highlights the stabilization effect of Li-rich material coating ($Li_{1.2}Ni_{0.2}Mn_{0.6}O_2$) on $LiNi_{0.7}Co_{0.15}Mn_{0.15}O_2$. The coated sample with 20 wt. % of $Li_{1.2}Ni_{0.2}Mn_{0.6}O_2$ (yellow line) shows improved cyclability with a capacity retention of 93 % during 100 cycles, while the bare material ($LiNi_{0.7}Mn_{0.15}Co_{0.15}O_2$, yellow line) has a capacity retention of 80 %. However, Li-rich materials need high charge voltage (at least 4.6 V) to activate its Li_2MnO_3 phase that plays a key role in realizing high capacity. As a result, the coated sample with 20 wt. % of $Li_{1.2}Ni_{0.2}Mn_{0.6}O_2$ has a lower discharge capacity than the bare sample Figure I-12. Therefore,

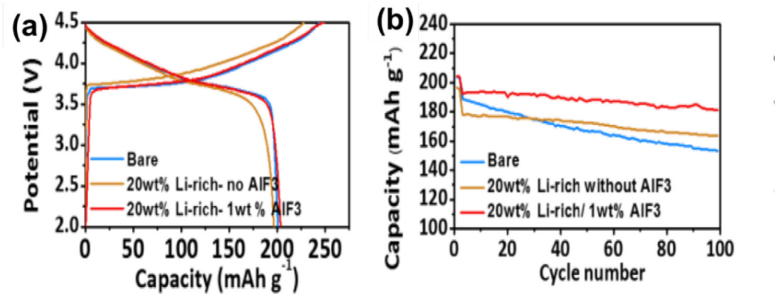

Figure I-12: (a) Voltage profiles of bare and coated samples between 2.0 and 4.5 V at C/10 rate (= 20 mA g^{-1}) at 25 °C. (b) Cycle performance during 2 initial cycles at C/10 rate and further 98 cycles at C/3 rate.

to prevent the decrease in the capacity of the coated material, we need to activate the Li_2MnO_3 phase before utilization. To do so, we applied chemical activation to activate the surface Li_2MnO_3 phase instead of electrochemical activation with the charge process of above 4.6 V, because Ni-rich material undergoes severe phase degradation from layered to NiO rock salt structure at above 4.6 V. (Chemical activation method denotes

Li extraction using acidic or basic chemical solvent.) In this experiment, we conducted chemical activation on Li-rich coated Ni-rich materials using AlF_3 sub-coating, which is a well-known coating material as both a stabilizing and activation agent for Li-rich materials. As a result of the AlF_3 treatment, the double-coated sample with 20 wt. % of $Li_{1.2}Ni_{0.2}Mn_{0.6}O_2$ and 1 wt. % of AlF_3 (red line) shows a high discharge capacity of 210 mA h g^{-1} with good cycle performance of 94 % retention during 100 cycles.

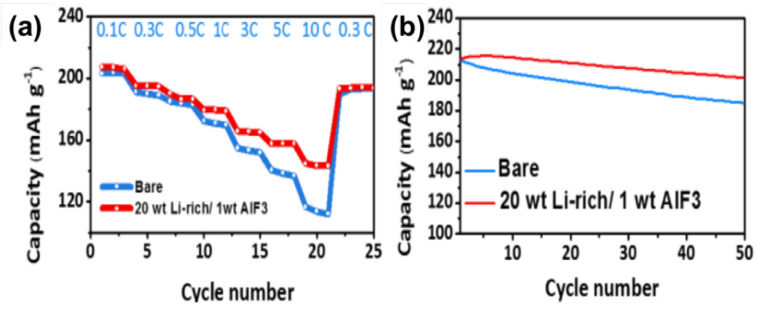

Figure I-13: (a) Rate capabilities of bare and coated samples with increasing C-rates from C/10 to 10C rate between 2.0 and 4.5 V at 25 °C, and (b) cycle performance during 100 cycles at 1C rate and 55 °C.

Furthermore, the double coating with $Li_{1.2}Ni_{0.2}Mn_{0.6}O_2$ and AlF_3 results in superior cycle performance at elevated temperatures and rate capability. The rate and cycle results are shown in Figure I-13, respectively. The double-coated sample shows a higher discharge capacity of 145 mA h g^{-1} at 10C rate compared to a lower discharge capacity of 112 mA h g^{-1} for the bare, uncoated sample. The superior rate property of the coated sample is due to the surface electrochemical stability that comes from the protecting effect of the surface coating layer. The double coating layer alleviates the surface instability of the Ni-rich material by reducing the unstable side reaction with electrolyte, which is the main reason for thick SEI layer formation and structural degradation of Ni-rich materials.

Li-rich layered Li_2MnO_3 is more stable towards carbonate-based nonaqueous electrolytes than the Ni-rich layered phase with a high cut-off voltage, such as 4.8 V *vs.* Li/Li^+. This is due to the less oxidizing surface Mn^{4+} ions (than Ni^{4+}) at highly delithiated states. Thus, a strategy based on a chemical formula of $xLi_2MnO_3 \cdot (1-x)LiNi_{0.7}Co_{0.15}Mn_{0.15}O_2$ is proposed to stabilize the local structure aiming for enhanced cyclability. A typical preparation procedure is quite simple, involving mixing the as-prepared $LiNi_{0.7}Co_{0.15}Mn_{0.15}O_2$ precursor with a stoichiometric amount of $MnCO_3$ and $LiOH \cdot H_2O$ according to various x values, followed by heat treatment at 500 and 800 °C. For the obtained $0.07Li_2MnO_3 \cdot 0.93LiNi_{0.7}Co_{0.15}Mn_{0.15}O_2$, we conducted long-term cycling tests in both coin half cell and laminated pouch full cell under C/3. As shown in Figure I-14, at 25 and 55 °C, 90.3 and 81.3 % of capacity retention, respectively, after 400 and 200 cycles cycled have been obtained, by taking advantages of the stabilized surface by Li_2MnO_3 formation. Additionally, 87.7 % capacity retention after 170 cycles for laminated pouch full cell fabricated with graphite anode was also achieved. All the results show that the combination of Li_2MnO_3 and Ni-rich material can improve the stability of Ni-rich material.

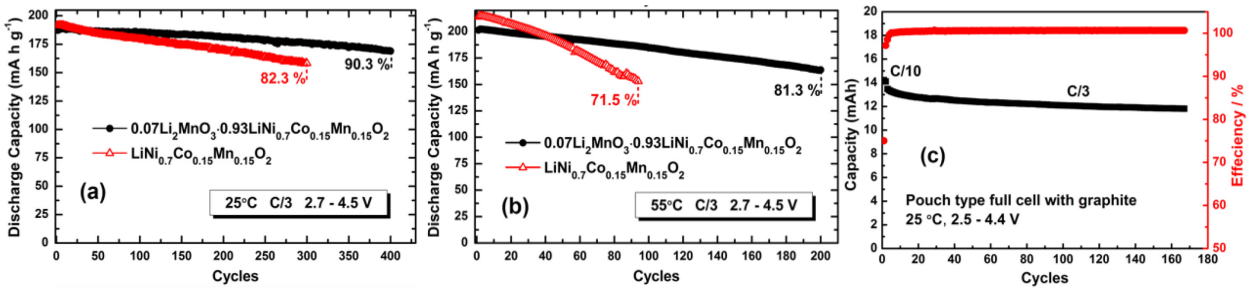

Figure I-15: Cycling performance of the pristine $LiNi_{0.7}Co_{0.15}Mn_{0.15}O_2$ and surface-modified $0.07Li_2MnO_3 \cdot 0.93LiNi_{0.7}Co_{0.15}Mn_{0.15}O_2$ samples in 1.2 M $LiPF_6$ in a 3 : 7 mixture of ethylene carbonate (EC) and ethylmethyl carbonate (EMC) electrolyte at (a) 25 ºC and (b) 55 ºC, and (c) cycling test of $0.07Li_2MnO_3$-$0.93LiNi_{0.7}Co_{0.15}Mn_{0.15}O_2$ in laminated-type pouch graphite full cells at 25 ºC.

3. Development of optimized concentration-gradient $LiNi_{0.76}Co_{0.10}Mn_{0.14}O_2$ (CG) cathode material

In order to further improve the performance and reach the project goal of cathode materials, concentration-gradient (CG) nickel-rich materials were investigated systematically. The research focused on the effect of different parameters on the performance, including element ratio, element distribution, particle size, base agent, and pH value. The research results showed that the best CG material is $LiNi_{0.76}Co_{0.1}Mn_{0.14}O_2$ that was prepared at a pH value of ~ 11.2 and that has a diameter of ~13 µm and a composition distribution of continuously decreasing Ni content, increasing Mn, and constant Co content from the interior to the surface.

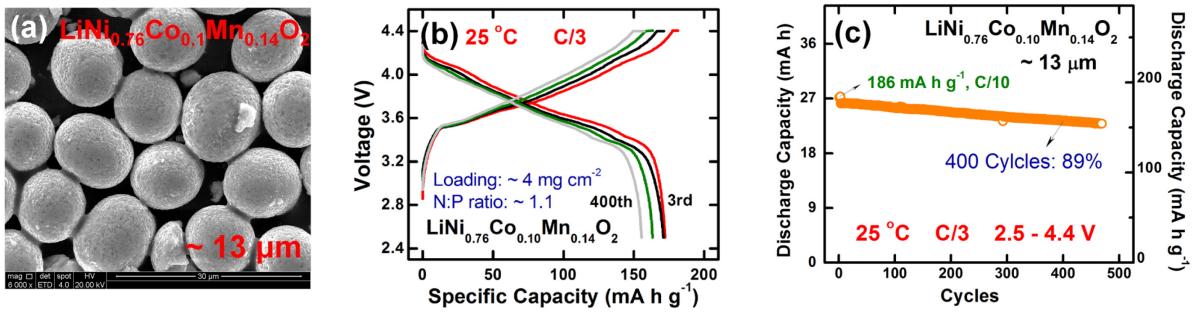

Figure I-15: (a) SEM image of $LiNi_{0.76}Co_{0.10}Mn_{0.14}O_2$ (CG). (b) Galvanostatic charge-discharge curves and (c) capacity evolution of the sample as a function of cycles in pouch-type full cells with ~ 4 mg cm^{-2} mass loading.

We have delivered one kilogram of the optimized concentration-gradient $LiNi_{0.76}Co_{0.1}Mn_{0.14}O_2$ (CG) cathode material for the project through transition-metal co-precipitation with precise composition and morphology control. In Figure I-15a, it can be seen that the sample consists of uniform spherical particles of around 13 µm. The electrochemical performance of the CG material was evaluated in pouch full cells at room temperature with a ~ 4 mg cm^{-2} mass loading. Figure I-15b, and 15c show the evolution of galvanostatic charge-discharge profiles and specific discharge capacity, respectively, as a function of cycles. It can be seen that the sample delivered a discharge capacity of 186 mA h g^{-1} at C/10 (C = 180 mA g-1) and retained ~ 89% of its initial discharge capacity after 400 cycles within the voltage window of 2.5 – 4.4 V vs. Li/Li^+. The over-potentials during cell operation, as demonstrated by the charge-discharge curves in Figure I-15b, are noticeable, although the sample has been surface-modified to suppress various interfacial side reactions.

Electrolyte

With the new batch of anode from PSU, PSU_1000_30, we investigated the performance of 10% FEC as an additive in the EC and EMC based electrolyte (1.2M LiPF6 in EC/EMC=3/7 in weight ratio). The anode half cell using that electrolyte was tested. The voltage window was set from 0.005V to 1.5V at room temperature. The first formation cycle was under the rate of 0.1C and the rest of cycling life was tested under 0.2C. SEM image of the pristine anode electrodes are shown in Figure I-16 and no morphology difference with pervious batch was observed.

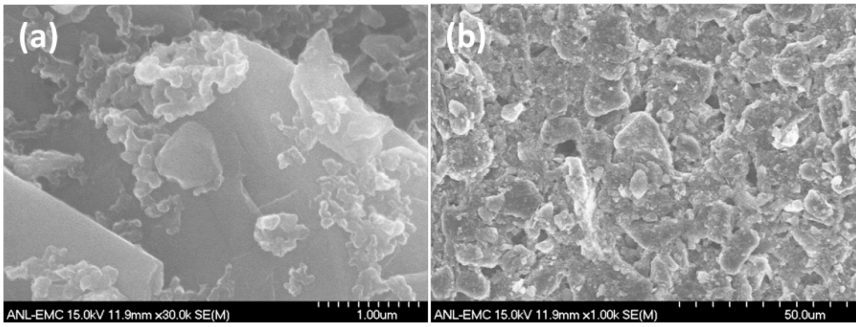

Figure I-17: SEM characterization of pristine Si anode from PSU in different magnification. (a). High magnification (b). Low magnification.

The cycling performance of PSU_1000_30 is shown in Figure I-17a and 17b. Two electrodes showed good capacity retention. The first cycle's Coulombic efficiency of the first sample is 72.68% and 72.67% of the second sample. Both of them are higher than the last batch PSU600 and PSU800 sample half cells. After the first few cycles, the Coulombic efficiency of both electrodes were stabilized on 99.5%. The area capacity of the first sample was stabilized on 5mAh/cm2 and 4.2mAh/cm2 for the second sample.

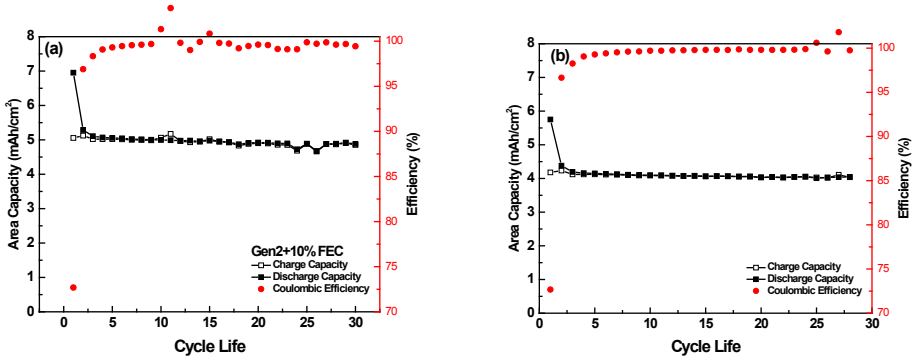

Figure I-17: Capacity retention and Coulombic efficiency of PSU anode /Li half cells with baseline electrolyte (a) PSU_1000_30 sample 1. (b) PSU_1000_30 sample 2.

Due to the PSU_1000_30 sample shows a good capacity retention on the half cell, we try to assemble the PSU_100_30/LiNi0.5Mn0.3Co0.2O2 full cell in Argonne to further investigate the performance of the anode. The LiNi0.5Mn0.3Co0.2O2 electrode (AC013 batch) was fabricated in Argonne national lab by CAMP facility. The cycling data of AC013/Li half cells in different cut off voltage with Gen 2 electrolyte are shown in Figure I-17. Under a 4.4V cutoff voltage, the cell shows a good capacity retention and the area capacity was stabilized on 2.0mAh/cm2. When we increased the cutoff voltage from 4.4V to 4.6V, a higher area capacity, 2.4 mAh/cm2, can be got. However, the capacity retention was not comparable with the 4.4V data.

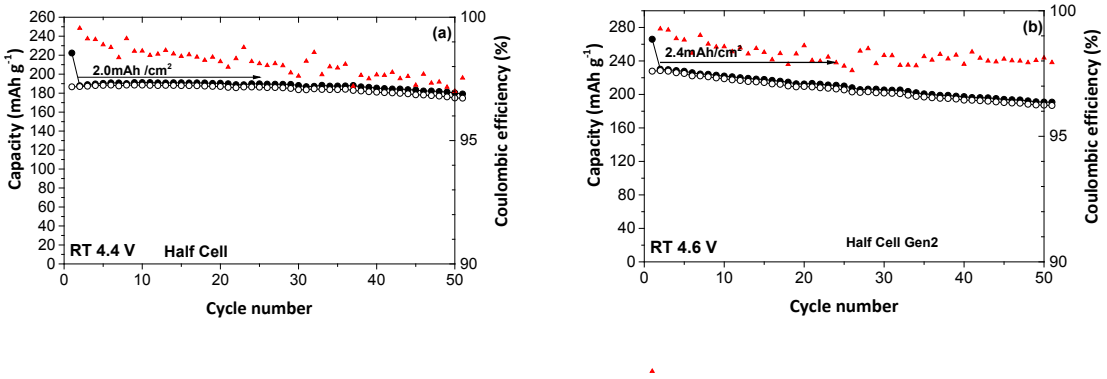

Figure I-18: Capacity retention and Coulombic efficiency of AC013/Li half cells with Gen 2 electrolyte in different cutoff voltage. (a). 3.0 V-4.4V, (b). 3.0V-4.6V.

Based on the half cell data we have, we begin testing the full cell with PSU100_30 anode and AC013 cathode under 4.5V cut off voltage in different electrolyte. Figure I-19 and b show the capacity retention and Coulombic efficiency of the full cell in Gen2 and Gen2+10% FEC electrolyte. Both of the two cells shows a low first cycle Coulombic efficiency, 42.9% for the Gen2 one and 41.8% for the Gen2+10% FEC one. The low first cycle's Coulombic efficiency were result from a high areal capacity ratio of negative to positive electrodes (N/P ratio). The N/P ratio is one of the most important factors to design the lithium ion batteries with high performance in the consideration of balanced electrochemical reactions. Based on our pervious study, the cell with 1.1 to 1.20 of N/P ratio shows the enhanced cycle performance in comparison with other cells. A low N/P ratio may cause the lithium plating on the anode side and a high N/P ratio will lead to a low first cycle's Coulombic efficiency due to the loss of Li ion on the formation of SEI step.

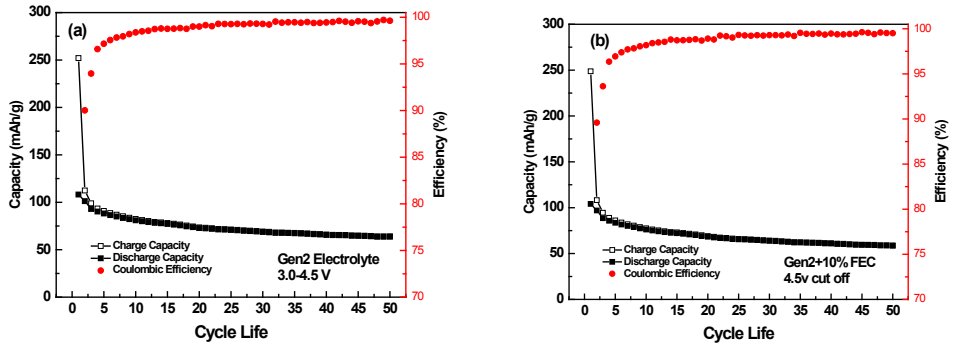

Figure I-19: Capacity retention and Coulombic efficiency of PSU_1000_30/ AC013 full cell under 4.5V cutoff voltage in different electrolyte (a) Gen2 electrolyte (b) Gen2+10% FEC electrolyte.

Prelithiation

1. Prelithiation Effect in SiO/NMC Full Cell

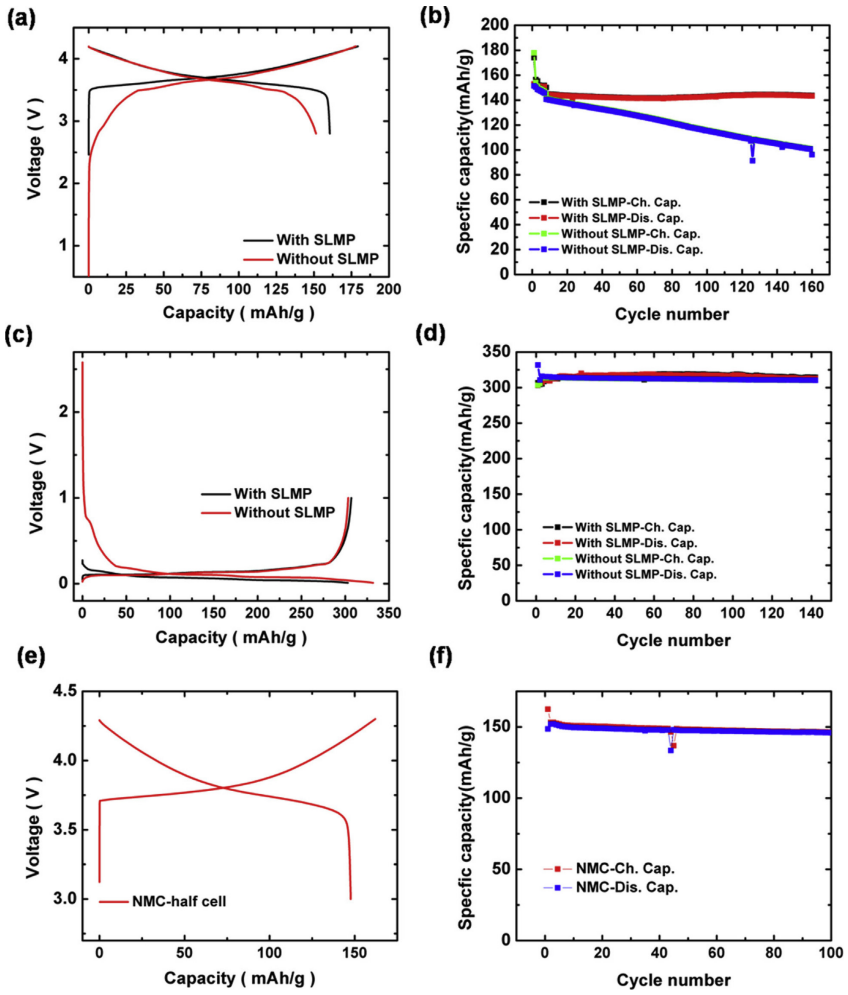

Figure I-20. The voltage profile for the first cycle (a), and cycling performance (b) for a graphite/NMC full cell, the first-cycle voltage (c), and cycling performance (d) for graphite half cell and the first-cycle voltage (e), and cycling performance (f) NMC half cell. The performance of each cell both with and without SLMP prelithiation is plotted in (aed).

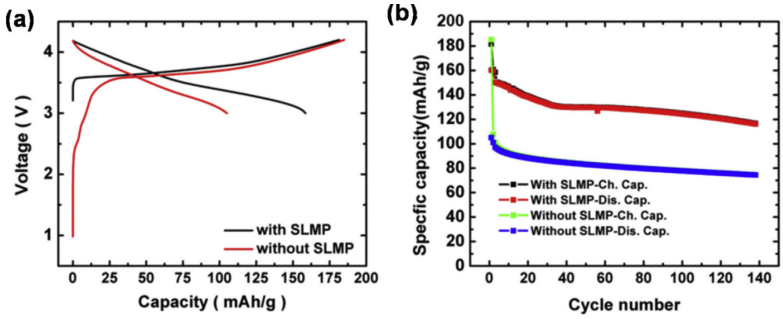

Figure I-21. The voltage profile for the first-cycle (a) and cycling performance (b) for SiO/NMC full cell.

The prelithiation of SLMP becomes crucially important in high energy density anode, such as Si or SiO, etc., because of their up to 40%-50% first cycle coulombic loss. The prelithiation effect of SLMP is demonstrated by SiO/NMC full cell with the solution processing method of SLMP coating, Figure I-21. The SiO anode is composed of SiO nanoparticle (95 wt.%) with conductive binder (PFM, 5 wt.%). Significant improvement is observed in the SLMP prelithiated full cells, Figure I-21 (b). The first cycle CE increases from 56.78% (without SLMP prelithiation) to 88.12% (with SLMP prelithiation) with this solution processing method. This is because that, in the full cell design, the lithium ion in the cathode is accurately calculated to match the capacity of the anode and not much excess lithium ion exists. The formation of SEI in the first few cycle will consume most of the excess lithium ion and the long term cycle ability will suffer due to the lithium ion loss. What's more, the lithium ion consumption during the SEI formation is a lot higher in the SiO anode than in

graphite anode. So without the prelithiation of SLMP, the SiO/NMC full cell can only start with a capacity of ~110 mAhg-1 and dropped to ~80 mAhg-1 after 100 cycles (based on cathode weight). While with the prelithiation of SLMP, the SiO/NMC full cell can maintain a reversible capacity of 130 mAhg-1 for over one hundred cycles. Therefore, with the coating of SLMP onto the anode of the full cell, well calculated amount of lithium ion is added into the system and compensates the lithium ion loss during SEI formation. In this way, a much prominent improvement in cycle ability can be observed in SiO/NMC full cell.

2. Baseline for Si/Graphite composite anode.

The above work established a polymer solution dispersion method to coat SLMP onto the SiO electrode surface to improve Coulombic efficiency. The morphology of the SLMP coated electrodes were collected through SEM observation. The morphology study showed that SBR solution enables a uniform distribution of SLMP coating, polystyrene (PS) helps the activation of SLMP after electrolyte addition. Based on configuration of SiO electrode, Si based electrode is scheduled here. Prior the integration of SLMP, Si/graphite composite half cells were evaluated as control as below:

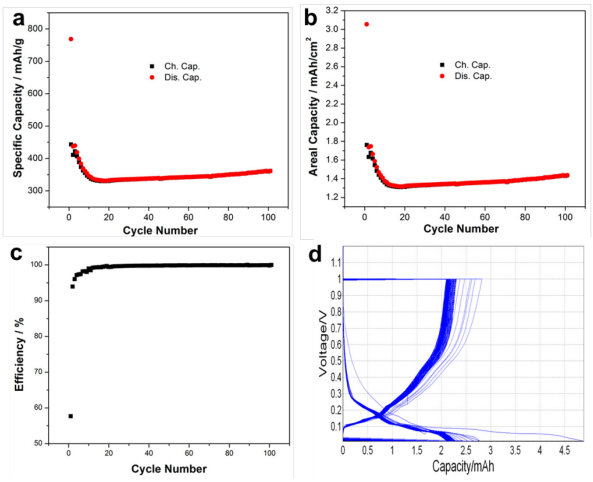

Figure I-22 Cycling performance of Si-graphite composite between 1V and 0.01. The calculated theoretical capacity is 600 mAh/g with a coating thickness of 80 µm.

As shown in Figure I-35, charge-discharge cycling performed of Si/graphite anode with Li insertion theoretical capacity of 600 mAh/g showed stable performance for more than 100 cycles. At a current density of 0.1C, the reversible Li extraction specific capacity is in the range of 320 to 450 mAh/g. The corresponding areal capacity can reach between 1.3 and 1.8 mAh/cm2. The initial CE is around 58% and charge-discharge takes place around 0.5 and 0.4V.

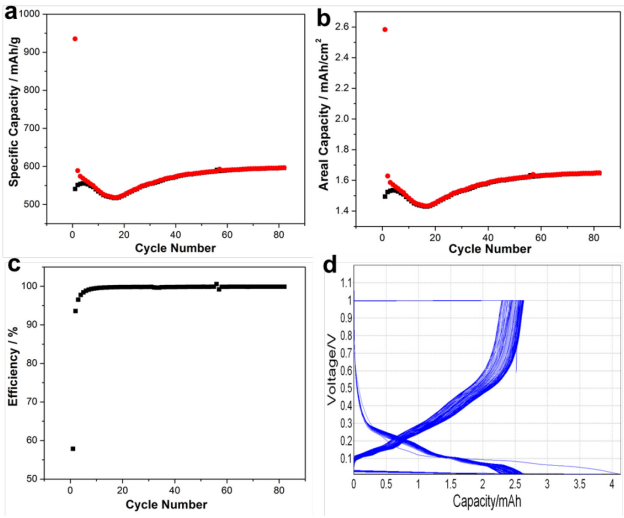

Figure I-23 Cycling performance of Si-graphite composite between 1V and 0.01. The calculated theoretical capacity is 800 mAh/g with a coating thickness of 60 µm.

To optimize the energy density, the ratio of Si was increased to possess a theoretical capacity of 800 mAh/g. The thickness of the electrode was controlled to 60 µm. Figure I-23 shows the galvanostatic measurements for this composite at 0.1 C. As displayed in Figure I-23a, over the whole range of 80 cycles, the composite shows 500 to 600 mAh/g capacities, which is higher than the composite with less Si. However, the areal capacity is similar, which ascribed to a relatively low mass loading. Hence, a higher loading performance is presented in Figure I-24 with the same Si graphite ratio to reach higher areal capacity. As expected, the areal loading in Figure I-24 bincreased to around 2.1 mAh/ cm2 when the coating thickness was increased to 80 µm. The initial CE for these two composite is both around 55%. Afterwards, the CE increases rapidly to more than 99.9% as shown in Figure I-24b and Figure I-24c.

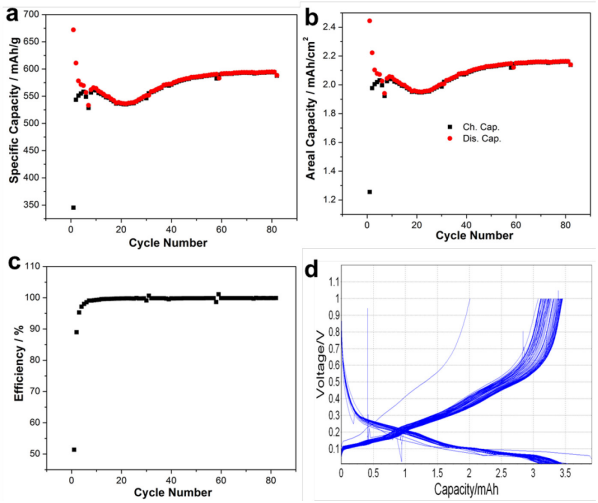

Figure I-24 Cycling performance of Si-graphite composite between 1V and 0.01. The calculated theoretical capacity is 800 mAh/g with a coating thickness of 80 µm.

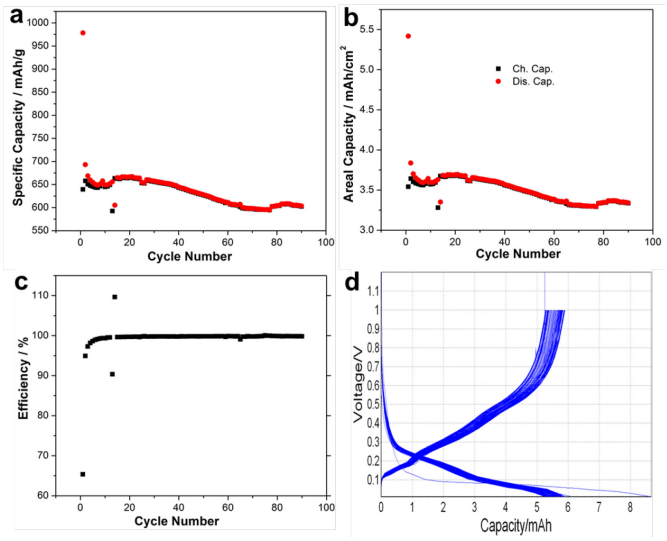

Figure I-25 Cycling performance of Si-graphite composite between 1V and 0.01. The calculated theoretical capacity is 1000 mAh/g with a coating thickness of 30 µm.

To reach a higher energy density, a composite anode with a higher Si content and a lower loading is fabricated. Within 100 cycles, the composite anode approach areal capacity of around 3.5 mAh/cm2 at rate of 0.1. (Figure I-25 b) Although the coulombic efficiencie slightly increase to more than 60%, it is still not adequate to fabricate a full cell. The nonideal Coulombic efficiencies likely result from repetitive SEI cracking and regeneration during cycling caused by huge volumetric changes in the Si.

All above, the study showed that excellent cycle performance can be achieved through the optimization of the ratio between Si and graphite and the electrode thickness modification. The performance make the optimized Si-graphite composite a good candidate for lithium ion batteries. However, the low CE issue should be addressed before the full cell test. Hence, a series of full cells with SLMP modified Si-graphite composite anode will be assembled in pouch cells with improved initial Coulombic efficiencies.

3. Application of SLMP in NMC/Si-C full pouch cell

Based on the Si/graphite half cell investigation, the Si-C ABR 1000 anode material is adopted to integrate with NMC to test in full pouch cell. The image of SLMP coating on anode electrode is shown in Figure I-26.

Figure I-26. SLMP coating on 12 cm2 pouch cell with the optimized disperse agent, i.e.m 0.5 wt% SBR and 0.5 wt% PST in xylene solution.

Final cell

1. Cell design

The cell design for Lithiated Si/C-Graphite / Ni Rich NCM Pouch Cell was developed. Since silicon has very high irreversible capacity, pre-lithiation is very necessary to achieve high energy density of pouch cells. We had three 3 types of cell fabricated in EC Power. Type 1 (Cells #1-18) uses Si anode and NCM523 cathode. Type 2 (UT-1 and UT-2) uses Si anode and Ni rich NCM cathode made by UT Austin. Type 3 (LiSi series) uses lithium powder coated Si anode and NCM523 cathode.

2. Cell fabrication

EC power fabricated 3 types of cell. Type 1 (Cells #1-18) uses Si anode and NCM523 cathode. Type 2 (UT-1 and UT-2) uses Si anode and Ni rich NCM cathode made by UT Austin. Type 3 (LiSi series) uses lithium powder coated Si anode and NCM523 cathode.

Totally 24 cells was fabricated. Table 1 lists the initial performance of these cells. Because anode has ~ 1.8 Ah irreversible capacity, all the Si/NCM523 and Si/Ni rich cells shows low capacity. Li coating can increase cell capacity a lot, but Li powder coating increase electrode thickness a lot. The weight of pouch cell using Li coated Si anode increases ~3 g and the cell thickness increases from 6.2 mm to 7.2 mm.

The specific energy of LiSi series cells can reach 190 Wh/kg. The specific energy of Si-Graphite / NCM523 cells are about 120 Wh/kg. Ni Rich NCM made by UT-Austin shows higher capacity than commercial NCM523. But particle size of UT-Austin NCM is not uniform. Roll to roll electrode coating using this material is very difficult.

Table 1. Initial performance of ABR cells *

Cell No.	HFR after filling, mΩ	1st charge capacity @ current=	1st discharge capacity @ current=0.22 A, Ah	2nd charge capacity @ current=	2nd discharge capacity @ current=0.16 A, Ah	Pouch cell weight, g	Pouch cell thickness, mm

		0.22 A, Ah		0.16 A, Ah			
1	64.53	2.946	1.247	1.439	1.328	40.83	6.2
2	57.23	2.877	1.220	1.392	1.287	41.17	
3	52.35	2.917	1.200	1.37	1.306	41.16	
4	54.73	2.835	1.189	1.921	1.19	40.29	
5	56.87	2.837	1.129	1.254	1.358	41.32	
6	62.21	2.798	1.180	1.384	1.291	40.65	
7	68.34	2.914	1.194	1.32	1.257	39.83	
8	60.33	2.926	1.233	1.454	1.365	40.81	
9	60.03	2.944	1.264	1.446	1.369	41.16	
10	60.48	2.912	1.304	1.512	1.429	40.72	
11	57.03	2.921	1.214	2.851	1.233	41.3	
12	66.38	2.825	1.247	1.465	1.384	40.68	
13	53.51	2.844	1.165	1.399	1.267	40.83	
14	47.98	2.913	1.265	1.418	1.278	41.53	
15	57.89	2.937	1.245	1.443	1.317	41.11	
16	63.57	2.959	1.239	1.403	1.278	41.18	
17	55.39	2.864	1.231	1.418	1.327	40.5	
18	51.95	2.884	1.235	1.427	1.31	40.83	
UT-1	42.77	3.231	1.388	1.929	1.447	41.13	6.3
UT-2	42.77	3.310	1.520	1.724	1.543	41.23	
LiSi-1	71.89	1.800	1.086	2.34	2.221	43.4	7.2
LiSi-2	70.80	2.819	2.079	2.239	2.294	43.81	
LiSi-3	64.10	2.696	2.033	2.197	2.236	44.06	
LiSi-4	59.26	2.820	1.870	2.3	2.321	44.01	

* Charge/Discharge window: 4.2V/2.7V.

Figure I-27. Photos of the final delivered full cell.

Figure I-27 shows stacking package, top view and side view the full cell. just before top sealing and the front view of pouch cells produced by EC Power. Sealing is perfect. Surface is very smooth. The cell is very hard. 14 pieces of double-side coating anode and 15 pieces of cathode (13 double side coating and 2 single-side coating cathode) was assembled. Nickel tab was welded with copper current collector. Aluminum tab was welded with aluminum current collector. The cell thickness is very uniform.

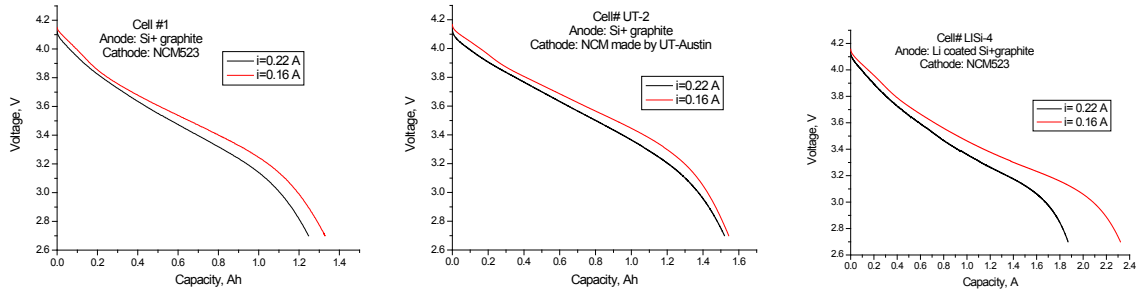

Figure I-28. Voltage profile of the first cycles of cell #1, cell# UT-2 and cell# LiSi-4 at discharged states.

3. Cycle performance

Figure I-28 shows capacity of cell #1 at different discharge current. The cell capacity is 1.328 Ah at discharge current of 0.16 A. Figure 6 shows capacity of cell# UT-2. Nickel rich NCM made by UT-Austin is used as cathode active material. The cell capacity using UT-Austin NCM is high than that using commercial NCM523. Figure 7 shows capacity of cell# LiSi-4. Because there are some Li power peeled off, anode has ~ 0.8 Ah irreversible capacity (designed irreversible capacity: 0.4 Ah), the cell capacity still a little lower than designed value.

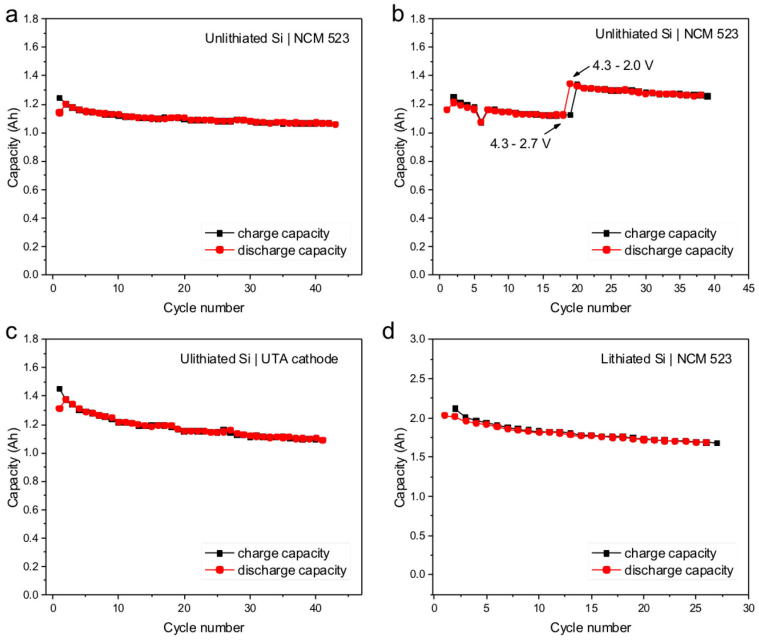

Figure I-29: Cycling performances of three types of full cell systems: a,b) Unlithiated Si| NCM523 with two kinds of voltage winodw, c) unlithiated Si| UTA cathode and d) Lithiated Si| NCM523.

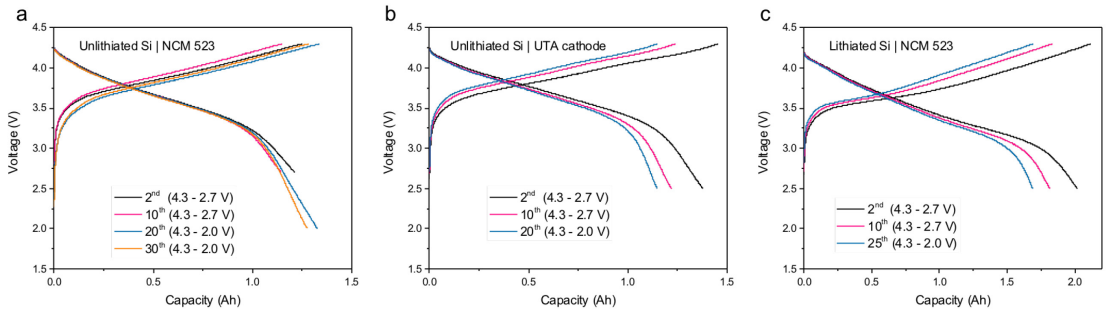

Figure I-30: Voltage profiles of three types of full cell systems: a) Unlithiated Si| NCM523, b) unlithiated Si| UTA cathode and c) Lithiated Si| NCM523.

As shown in Figure I-29 and I-45, unlithiated Si| NCM523 cell and unlithiated Si| UTA cathode show the capacity of 1.3 Ah and 1.5 Ah. The lithiated cell presents 2.2 Ah due to the prelithiation. All cells exhibit good cyclability under 4.3- 2.7 V voltage window and 4.3 – 2.0V voltage window.

Conclusions

High-loading and high quality PSU Si anode has been optimized and fabricated. The electrochemical performance has been utilized. The PSU Si-graphite anode exhibits the mass loading of 5.8 mg/cm2, charge capacity of 850 mAh/ g and good cycling performance. This optimized electrode has been used for full-cell fabrication.

The performance enhancement of Ni-rich materials can be achieved by a diversity of strategies. Higher Mn content and a small amount of Al doping can improve the electrochemical performance by suppressing interfacial side reactions with electrolytes, thus greatly benefiting the cyclability of the samples. Also, surface coatings of Li-rich materials and AlF_3 are able to improve the performance stability of Ni-rich cathodes. One kilogram of optimized concentration-gradient $LiNi_{0.76}Co_{0.10}Mn_{0.14}O_2$ (CG) with careful control of composition, morphology and electrochemical performance was delivered to our collaborators. The sample achieved an initial specific capacity close to 190 mA h g^{-1} at C/10 rate and 180 mA h g^{-1} at C/3 rate as well as good cyclability in pouch full cells with a 4.4 V upper cut-off voltage at room temperature.

Electrolyte additive with Si-N skeleton forms a less resistant SEI on the surface of silicon anode (from PSU) as evidenced by the evolution of the impedance at various lithiation/de-lithiation stages and the cycling data

The prelithiation result demonstrates a solution processing method to achieve large area, uniform SLMP coating on well-made anode surface for the prelithiation of lithium-ion batteries. The prelithiation effect with this method is applied both in graphite half cells, graphite/NMC full cells, SiO half cells, SiO/NMC full cells, Si-Graphite half cells and Si-Graphite/NMC full cells with improvements in cycle performance and higher first cycle coulombic efficiency than their corresponding cells without SLMP prelithiation.

As to the full cell fabrication and test, full pouch cells with high capacity of 2.2 Ah and 1.2 Ah have been fabricated and delivered. The cells show great uniformity and good cycling performance. The prelithiation method effectively compensate the loss in the first cycle. The cell with high energy density and long-cycle life has been achieved.

I.1.A.3. Products (Heading 4)

Presentations/Publications/Patents (APR_Gray Shaded_Heading)

Publications:

1. J.-Y. Liao and A. Manthiram, “Surface-modified Concentration-gradient Ni-rich Layered Oxide Cathodes for High-energy Lithium-ion Batteries,” *Journal of Power Sources* **282**, 429-436 (2015).

2. J. Zheng, W. H. Kan, and A. Manthiram, "Role of Mn Content on the Electrochemical Properties of Nickel-rich Layered $LiNi_{0.8-x}Co_{0.1}Mn_{0.1+x}O_2$ ($0.1 \leq x \leq 0.18$) Cathodes for Lithium-ion Batteries," *ACS Applied Materials & Interfaces* **7**, 6926-6934 (2015).
3. A. Manthiram, J. C. Knight, S.-T. Myung, S.-M. Oh, and Y.-K. Sun, "Nickel-rich and Lithium-rich Layered Oxide Cathodes: Progress and Perspectives," *Advanced Energy Materials* **1501010**, 1-23 (2015).
4. J. Zheng, P. Yan, W. H. Kan, C. Wang, and A. Manthiram, "A Spinel-integrated P2-type Layered Composite: High-rate Cathode for Sodium-ion Batteries," *Journal of the Electrochemical Society* **163**, A584-A591 (2016).
5. P. Oh, B. Song, W. Li, and A. Manthiram, "Overcoming the Chemical Instability on Exposure to Air of Ni-rich Layered Oxide Cathodes by Coating with Spinel $LiMn_{1.9}Al_{0.1}O_4$," *Journal of Materials Chemistry A* **4**, 5839-5841 (2016).
6. P. Oh, S.-M. Oh, W. Li, S. Myeong, J. Cho, and A. Manthiram, "High-performance Heterostructured Cathodes for Lithium-ion Batteries with a Ni-rich Layered Oxide Core and a Li-rich Layered Oxide Shell," *Advanced Science* **1600184**, 1-8 (2016).
7. B. Song, W. Li, P. Yan, S.-M. Oh, C.-M. Wang, and A. Manthiram, "A Facile Cathode Design Combining Ni-rich Layered Oxides with Li-rich Layered Oxides for Lithium-ion Batteries," *Journal of Power Sources* **325**, 620-629 (2016).
8. J.-Y. Liao, S.-M. Oh, and A. Manthiram, "A Core/double-shell Type Gradient Ni-rich $LiNi_{0.76}Co_{0.10}Mn_{0.14}O_2$ with High Capacity and Long Cycle Life for Lithium-ion Batteries," *ACS Applied Materials and Interfaces* **8, 24543-24549** (2016).
9. W. Li, A. Dolocan, P. Oh, H. Celio, S. Park, J. Cho, and A. Manthiram, "Revealing the Interphases and Their Implications on High-energy-density Cathode Materials in Lithium-ion Batteries," *Nature Communications* (submitted).
10. Xiaodong Yan, Zhihui Wang, Min He, Zhaohui Hou, Ting Xia, Gao Liu, and Xiaobo Chen. TiO2 nanomaterials as anode materials for lithium-ion rechargeable batteries. Energy Technology, **2015**, 3, 801-814.
11. Hui Zhao, Zhe Jia(**co-first author**), Wen Yuan, Heyi Hu, Yanbao Fu, Gregory Baker, and Gao Liu. Fumed silica based single-ion nanocomposite electrolyte for lithium batteries. ACS Applied Materials & Interfaces, **2015**, 7, 19335-19341.
12. Kehua Dai, Zhihui Wang(**co-first author**), Guo Ai, Hui Zhao, Wen Yuan, Xiangyun Song, Vincent Battaglia, Chengdong Sun, Kai Wu, and Gao Liu. The transformation of graphite electrode materials in lithium ion batteries after cycling. J. Power Sources, **2015**, 298, 349-354.
13. Hui Zhao, Fadi Asfour(**co-first author**), Yanbao Fu, Zhe Jia,Wen Yuan, Ying Bai, Min Ling, Heyi Hu, Gregory Baker, and Gao Liu. Plasticized polymer composite single-ion conductors for lithium batteries.ACS Applied Materials & Interfaces, **2015**, 7, 19494-19499.
14. Ying Bai, Xingzhen Zhou, Zhe Jia, Chuan Wu, Liwei Yang, Mizi Chen, Hui Zhao, Feng Wu, and Gao Liu. Understanding the combined effects of microcrystal growth and band gap reduction of Fe(1-x)TixF3 nanocomposites as cathode materials for lithium-ion batteries. Nano Energy, **2015**, 17, 140-151.
15. Zhe Jia, Hui Zhao, Ying Bai, Ting Zhang, Amanda Siemens, Andrew Minor, and Gao Liu. Solvent processed conductive polymer with single-walled carbon nanotube composites. Journal of Materials Research, **2015**, Accepted.
16. Hui Zhao, Wei Yang, Ruimin Qiao, Chenhui Zhu, Ziyan Zheng, Min Ling, Zhe Jia, Ying Bai, Yanbao Fu, Jinglei Lei, Xiangyun Song, Vincent Battaglia, Wanli Yang, Phillip Messersmith, and Gao Liu. Conductive polymer binder for high-tap-density nano-silicon material for lithium ion battery negative electrode application. Nano Letters. **2015**, 15, 7927-7932.
17. Guo Ai, Zhihui Wang, Hui Zhao, Wenfeng Mao, Yanbao Fu, Vincent Battaglia, Sergey Lopatin, and Gao Liu. Scalable process for application of stabilized lithium metal powder in Li-ion batteries. Journal of Power Sources 309 (2016) 33-41.
18. He, Meinan, et al. "Mechanistic Insight in the Function of Phosphite Additives for Protection of LiNi0. 5Co0. 2Mn0. 3O2 Cathode in High Voltage Li-Ion Cells." ACS applied materials & interfaces 8.18 (2016): 11450-11458.

19. He, Meinan, et al. "Fluorinated Electrolytes for 5-V Li-Ion Chemistry: Probing Voltage Stability of Electrolytes with Electrochemical Floating Test." Journal of The Electrochemical Society 162.9 (2015): A1725-A1729.

Presentations:

1. A. Manthiram, "Materials for Next-Generation Rechargeable Batteries," *5th Association of East Asian Research Universities (AEARU) Advanced Materials Workshop*, Hong Kong, June 4, 2014 (invited).
2. A. Manthiram, "Electrochemical Energy Storage: Challenges and Prospects," *International Conference on Electrochemical Science & Technology (ICONEST-2014)*, Bangalore, India, August 7 – 9, 2014 (invited plenary talk).
3. A. Manthiram, "From Insertion-compound Electrodes to Conversion-reaction Electrodes for Energy Storage," Battery Division Research Award Presentation, *226th Electrochemical Society Meeting*, Cancun, Mexico, October 5 – 10, 2014 (invited).
4. A. Manthiram, "Next Generation Rechargeable Battery Chemistries," *XII International Congress of the Mexican Hydrogen Society*, Cancun, Mexico, September 30 – October 4, 2014 (invited keynote talk).
5. A. Manthiram, "Next Generation Rechargeable Battery Chemistries," 2014 Global Innovation Festival, Daegu Gyeongbuk Institute of Science and Technology, Daegu, South Korea, November 20 – 21, 2014 (invited).
6. A. Manthiram, "Rechargeable Batteries: Transitioning from Insertion-compound Electrodes to Conversion-reaction Electrodes," *International Symposium on Energy Conversion and Storage*, Beijing, China, May 31 – June 1, 2015 (invited).
7. A. Manthiram, "Prospects and Challenges of Nickel-rich Layered Oxide Cathodes," *2015 Annual Merit Review Meeting of the Office of Vehicle Technologies*, U.S. Department of Energy, Washington, D.C, June 8 – 12, 2015 (invited).
8. A. Manthiram, "Transitioning from Insertion-reaction Electrodes to Conversion-reaction Electrodes for Energy Storage," Lawrence Berkeley National Laboratory, Berkeley, CA, July 13, 2015 (invited).
9. A. Manthiram, "Structural and Electronic Stabilities of Oxide Cathodes for Lithium-ion Batteries," *5th Polish Forum on Smart Energy Conversion and Storage,* Bialka Tatrzanska, Poland, September 22 – 25, 2015 (invited).
10. A. Manthiram, "Electrical Energy Storage: Next Generation Battery Chemistries," *2015 International Conference on Innovative Electrochemical Energy Materials and Technologies (EEMT2015)*, Nanning, China, November 8 – 11, 2015 (invited plenary talk).
11. A. Manthiram, "Electrical Energy Storage: Materials Challenges and Prospects," *2015 Fall Meeting of the Materials Research Society*, Boston, MA, November 29 – December 4, 2015 (invited talk at Symposium X: Frontiers of Materials Research).
12. A. Manthiram, "Tutorial on Electrode Materials and Electrolytes for Next Generation Rechargeable Batteries," *2016 Spring Meeting of the Materials Research Society*, Phoenix, AZ, March 28, 2016.
13. A. Manthiram, Wangda Li, Jin-yun Liao, Jianming Zheng, "Advanced Surface Characterization and Surface-controlled Compositional Design of Nickel-rich Layered Oxide Cathodes for Lithium-ion Batteries," *2016 Spring Meeting of the Materials Research Society*, Phoenix, AZ, March 28 – April 1, 2016 (invited).
14. A. Manthiram, "Next Generation Battery Chemistries: Materials Challenges and Prospects," *Materials Challenges in Alternative and Renewable Energy (MCARE) Meeting*, Clearwater, FL, April 17 – 21, 2016 (invited plenary talk).
15. D. Wang and A. Manthiram, "High Energy, Long Cycle Life Lithium-ion Batteries for Vehicle Applications," *2016 Annual Merit Review Meeting of the Office of Vehicle Technologies*, U.S. Department of Energy, Washington, D.C, June 6 – 10, 2016.
16. A. Manthiram, "Materials for Electrochemical Energy Conversion and Storage Technologies," Indian Institute of Technology Madras, Chennai, India, August 16, 2016 (invited).
17. A. Manthiram, "Electrical Energy Storage: Next Generation Battery Chemistries," *4th International Workshop on Nanotechnology, Renewable Energy, and Sustainability,* Xi'an Jiaotong University, Xi'an, China, September 19, 2016 (invited keynote talk).

18. N, N-Diethyltrimethylsilylamine (DETMSA) As Electrolyte Additive for Si Based High Energy Lithium-Ion Batteries. Meinan He, Libo Hu, Yan Wang, Kang Xu and Zhengcheng Zhang. 227th ECS meeting, Chicago, May 24-28.
19. Donghai Wang, "Development of Stable Intermetallic Alloy Anodes for Li-ion/Na-ion Batteries," ACS National Spring Meeting, San Diego, March, 2016.
20. Donghai Wang, "Development of Functional Nanocomposite Materials for Energy Storage Applications" 11th Sino-US Nano Forum, Nanjing, China, 18-20 June, 2016.

Patents:

1. Scalable process for application of Stabilized Lithium Metal Powder in Li-ion Batteries, patent filed by Applied Materials Inc. on 2015
2. Wang, D. H., Song, J., Electroactive Polymer Binders with In-Situ Formation of Artificial Solid-Electrolyte-Interphase Layer for Si Anodes, U.S. Provisional Application (61/934,171), 2014

I.1.A.4. References

[1] J.B. Goodenough, Y. Kim, Chemistry of Materials, 22 (2010) 587-603.
[2] F.T. Wagner, B. Lakshmanan, M.F. Mathias, The Journal of Physical Chemistry Letters, 1 (2010) 2204-2219.
[3] J.M. Tarascon, M. Armand, Nature, 414 (2001) 359-367.
[4] Y. Dai, L. Cai, R.E. White, Journal of The Electrochemical Society, 160 (2013) A182-A190.
[5] Y. Dai, L. Cai, R.E. White, Journal of The Electrochemical Society, 161 (2014) E3348-E3356.
[6] Y. Dai, L. Cai, R.E. White, Journal of Power Sources, 247 (2014) 365-376.
[7] W.-f. Mao, Y. Ma, S.-k. Liu, Z.-y. Tang, Y.-b. Fu, Electrochimica Acta, 147 (2014) 498-505.
[8] W.-f. Mao, J. Yan, H. Xie, Z.-y. Tang, Q. Xu, Journal of Power Sources, 237 (2013) 167-171.
[9] G. Ai, Y. Dai, Y. Ye, W. Mao, Z. Wang, H. Zhao, Y. Chen, J. Zhu, Y. Fu, V. Battaglia, J. Guo, V. Srinivasan, G. Liu, Nano Energy, 16 (2015) 28-37.
[10] W.-f. Mao, Y.-b. Fu, H. Zhao, G. Ai, Y.-l. Dai, D. Meng, X.-h. Zhang, D. Qu, G. Liu, V.S. Battaglia, Z.-y. Tang, ACS Applied Materials & Interfaces, 7 (2015) 12057-12066.
[11] L. Ji, Z. Lin, M. Alcoutlabi, X. Zhang, Energy & Environmental Science, 4 (2011) 2682-2699.
[12] X.-L. Wu, Y.-G. Guo, L.-J. Wan, Chemistry – An Asian Journal, 8 (2013) 1948-1958.
[13] U. Kasavajjula, C. Wang, A.J. Appleby, Journal of Power Sources, 163 (2007) 1003-1039.
[14] Y. Bai, Y. Tang, Z. Wang, Z. Jia, F. Wu, C. Wu, G. Liu, Solid State Ionics, 272 (2015) 24-29.
[15] G. Liu, S. Xun, N. Vukmirovic, X. Song, P. Olalde-Velasco, H. Zheng, V.S. Battaglia, L. Wang, W. Yang, Advanced Materials, 23 (2011) 4679-4683.
[16] S.-J. Park, H. Zhao, G. Ai, C. Wang, X. Song, N. Yuca, V.S. Battaglia, W. Yang, G. Liu, Journal of the American Chemical Society, 137 (2015) 2565-2571.
[17] H. Zhao, Z. Wang, P. Lu, M. Jiang, F. Shi, X. Song, Z. Zheng, X. Zhou, Y. Fu, G. Abdelbast, X. Xiao, Z. Liu, V.S. Battaglia, K. Zaghib, G. Liu, Nano Letters, 14 (2014) 6704-6710.
[18] D.D. Vaughn Ii, R.E. Schaak, Chemical Society Reviews, 42 (2013) 2861-2879.
[19] M.W. Forney, M.J. Ganter, J.W. Staub, R.D. Ridgley, B.J. Landi, Nano Letters, 13 (2013) 4158-4163.
[20] V.A. Agubra, J.W. Fergus, Journal of Power Sources, 268 (2014) 153-162.
[21] X. Su, Q. Wu, J. Li, X. Xiao, A. Lott, W. Lu, B.W. Sheldon, J. Wu, Advanced Energy Materials, 4 (2014) 1300882.
[22] Y. Wang, H. Li, P. He, E. Hosono, H. Zhou, Nanoscale, 2 (2010) 1294-1305.
[23] J. Christensen, J. Newman, Journal of The Electrochemical Society, 152 (2005) A818-A829.
[24] D. Shanmukaraj, S. Grugeon, S. Laruelle, G. Douglade, J.M. Tarascon, M. Armand, Electrochemistry Communications, 12 (2010) 1344-1347.
[25] A. Ito, D. Li, Y. Sato, M. Arao, M. Watanabe, M. Hatano, H. Horie, Y. Ohsawa, Journal of Power Sources, 195 (2010) 567-573.
[26] C.R. Jarvis, M.J. Lain, Y. Gao, M. Yakovleva, Journal of Power Sources, 146 (2005) 331-334.
[27] C.R. Jarvis, M.J. Lain, M.V. Yakovleva, Y. Gao, Journal of Power Sources, 162 (2006) 800-802.
[28] B.B. Fitch, M. Yakovleva, Y. Li, I. Plitz, A. Skrzypczak, F. Badway, G.G. Amatucci, Y. Gao, ECS Transactions, 3 (2007) 15-22.
[29] J.T. Vaughey, G. Liu, J.-G. Zhang, MRS Bulletin, 39 (2014) 429-435.

[30] Y. Li, B. Fitch, Electrochemistry Communications, 13 (2011) 664-667.
[31] H. Zhao, N. Yuca, Z. Zheng, Y. Fu, V.S. Battaglia, G. Abdelbast, K. Zaghib, G. Liu, ACS Applied Materials & Interfaces, 7 (2015) 862-866.
[32] Z. Wang, Y. Fu, Z. Zhang, S. Yuan, K. Amine, V. Battaglia, G. Liu, Journal of Power Sources, 260 (2014) 57-61.
[33] X. Zhu, Y. Zhu, S. Murali, M.D. Stoller, R.S. Ruoff, ACS Nano, 5 (2011) 3333-3338.
[34] D.W. Murphy, P.A. Christian, F.J. DiSalvo, J.N. Carides, J.V. Waszczak, Journal of The Electrochemical Society, 128 (1981) 2053-2060.
[35] K.-W. Nam, S.-B. Ma, W.-S. Yoon, X.-Q. Yang, K.-B. Kim, Electrochemistry Communications, 11 (2009) 1166-1169.
[36] W.J. Cao, J. Shih, J.P. Zheng, T. Doung, Journal of Power Sources, 257 (2014) 388-393.
[37] L. Wang, Y. Fu, V.S. Battaglia, G. Liu, RSC Advances, 3 (2013) 15022–15027.
[38] F. Cassel, D. Chua, M. Lane, M. Yakovleva, Y. Gao, G. Au, ECS Transactions, 11 (2008) 157-166.
[39] F.J.V. Santos, C.A. Nieto de Castro, J.H. Dymond, N.K. Dalaouti, M.J. Assael, A. Nagashima, Journal of Physical and Chemical Reference Data, 35 (2006) 1-8.
[40] S. Singh, B.P.S. Sethi, R.C. Katyal, V.K. Rattan, Journal of Chemical & Engineering Data, 50 (2005) 125-127.